Green Chemistry

PAPER

View Article Online
View Journal | View Issue

Cite this: *Green Chem.*, 2025, **27**, 6105

Biomass-derived sustainable hypergolic rocket propellants with hydrogen peroxide†

Ramlithin Mavila Chathoth,[a] Charlie Oommen,[a] Michael Gozin,[b,c,d] Srinivas Dharavath,[e] Manojkumar Jujam,[e] Deepan Chowdhury[b] and Jagadish Das *[f]

Received 15th January 2025,
Accepted 17th April 2025

DOI: 10.1039/d5gc00255a

rsc.li/greenchem

Sustainable fuels, derived from various renewable biological sources, are having a significant impact on land and marine transportation, as well as on aviation. However, in the case of the space sector, this advancement is limited. In an effort to prepare a sustainable rocket fuel (SRF) from readily available bioresources, herein we report for the first time the valorization of a widely available biomass – coconut husk into hypergolic composite fuel. We showed that the hypergolic reactions of various formulations of coconut husk-derived SRFs with a green oxidizer – H_2O_2 (95%) could be promoted with the addition of catalytic amounts of guanine-containing polymeric complexes of manganese or copper (**Mn–GU** or **Cu–GU**). It was found that the top-performing fuel formulation, with a total manganese content of just 2 wt%, showed an impressive ignition delay time below 50 ms. Mechanistic studies exploring the structure–ignition capability relationships of coconut husk-derived SRFs and **Mn–GU** and **Cu–GU** materials revealed that the nitrate content of coconut husk-derived SRFs and the metal–ligand cooperation in the **Mn–GU** and **Cu–GU** complexes played important roles in the ignition process of our novel SRF formulations.

Green foundation

1. The traditional ammonium perchlorate-based rocket propellants, highly toxic and carcinogenic hydrazine, and corrosive fuming nitric acid/nitrogen tetroxide-based propellants produce environmentally hazardous greenhouse gases and chlorinated combustion products. In contrast, hydrogen peroxide (H_2O_2) produces only water and oxygen as green decomposition products. Therefore, developing H_2O_2-based propulsion systems is highly desired for future green space missions.
2. Herein, we have developed novel chlorine-free composite materials utilizing renewable biomass coconut-husk-derived fuel and guanine-derived metal complexes that exhibit excellent hypergolic ignition with a green oxidizer – H_2O_2. The study of the materials' ignition, energetic, and physical properties showed that they have the potential to be used as green and non-hazardous hypergolic propellants in hybrid rocket motors.
3. The present work will pave the way for the development of other renewable biomass-derived advanced green rocket propellants that will have higher performance than traditional rocket propellants.

Introduction

In recent years, the global space industry has seen exponential growth due to the rapid rise in the deployment of novel satellite technologies for both civil and defense applications, including surveillance, weather monitoring, global positioning, internet, and even cellular connectivity.[1,2] In 2023, the space economy was valued at $0.63 trillion, and it is anticipated to increase at a compound annual growth rate (CAGR) of 9%, reaching $1.80 trillion by 2035.[3] Due to the rapid increase in the pace and number of satellites launched, it is estimated that by the year 2050, the level of ozone layer depletion as a result of these launches could be much higher than that ever done by restricted-for-use chlorofluorocarbons (CFCs).[4] Therefore, there is a high demand for greener and sustainable

[a]*Department of Aerospace Engineering, Indian Institute of Science, Karnataka 560012, India*
[b]*School of Chemistry, Faculty of Exact Sciences, Tel Aviv University, Tel Aviv 69978, Israel*
[c]*Center for Nanoscience and Nanotechnology, Tel Aviv University, Tel Aviv 69978, Israel*
[d]*Center for Advanced Combustion Science, Tel Aviv University, Tel Aviv 69978, Israel*
[e]*Department of Chemistry, Indian Institute of Technology Kanpur, Kanpur 208016, Uttar Pradesh, India*
[f]*Department of Chemistry, Indian Institute of Technology Patna, Bihar 801106, India. E-mail: jdas@iitp.ac.in*
†Electronic supplementary information (ESI) available. See DOI: https://doi.org/10.1039/d5gc00255a

propulsion systems that can reduce harmful air pollutants and greenhouse gases arising from the burning of tons of traditional propellants.[5,6]

One of the propulsion systems used in spacecraft is based on a hypergolic reaction between a fuel and an oxidizer. The hypergolic reaction is a spontaneous, exothermic redox reaction that occurs when a suitable oxidizer is mixed with an appropriate liquid or solid fuel, leading to the ignition of the fuel. Such hypergolic propulsion systems could be advantageous as they eliminate the need for a separate igniter and can even offer higher performance with better control depending on the choice of fuel and oxidizer.[7–9] For hypergolic propulsion systems, hydrazine and its derivatives [monomethylhydrazine (MMH) and unsymmetrical dimethylhydrazine (UDMH)] are commonly used as fuels, and nitrogen tetroxide (N_2O_4) or fuming nitric acid (HNO_3) is used as an oxidizer.[10,11] These fuels are highly toxic and harmful to humans and the environment, and the oxidizers are highly corrosive, which creates severe problems in use, handling, storage, and disposal.[12] In an effort to develop more advanced semi-green hypergolic propulsion, energetic ionic liquids (EILs), metal organic frameworks (MOFs), and metal carborane clusters were studied as hypergolic fuels for their ignition with fuming HNO_3.[13–21] To further achieve a "fully green" propulsion system, several green oxidizers were recently investigated including hydroxylammonium nitrate (HAN), ammonium dinitramide (ADN), and hydrogen peroxide (H_2O_2).[22–27] Several groups reported that the hypergolic reaction of H_2O_2 (>90%) was achieved with some fuels including borohydride, cyanoborohydride, amino-borane, or bis-borane compounds.[28–51] Since H_2O_2 produces only water and oxygen during its decomposition, H_2O_2 is considered as the next-generation green oxidizer. The use of H_2O_2 as an oxidizer has many other advantages in terms of its relatively low cost, handling, storage, and disposal, in comparison with N_2O_4 and HNO_3.[52,53]

Recent studies showed that air- and water-stable transition metal complexes of energetic nitrogen-rich ligands exhibited impressive capability to promote hypergolic reactions with H_2O_2 (98%).[54,55] However, these complexes' relatively high cost and higher metal content (>15 wt%) may hamper their application in the next-generation sustainable hypergolic propulsion systems. One of the innovative solutions to this problem could be the utilization of agricultural waste and other biomasses to prepare cost-effective, green, and sustainable rocket fuels.

Bioenergy that could be obtained from biomass is an important pillar of a circular economy, which presently accounts for 55% of all global renewable energy supply and is about 6% of total energy produced worldwide.[56] The emission of greenhouse gases from fossil fuels is much higher than that from biofuels, which has triggered prolific and intense research related to the development of cost-effective processes for biomass conversion.[57,58] The advantages of using renewable biomass are that these feedstocks are available in huge quantities, including agricultural waste, forestry and wood processing residues, food waste, algae, and many others.[59–61] Due to microalgal and lignocellulose abundance, low cost, and non-edibility, these biomaterials are considered among the most promising feedstocks for the production of biofuels for land and marine transportation, as well as for sustainable aviation fuels (SAFs).[62,63]

The currently utilized processes for the latter feedstocks' conversion into biofuels are based on thermochemical processes that include hydrothermal liquefaction (HTL) and gasification, and on biochemical processes, such as fermentation (ethanol production) and anaerobic digestion (biogas production).[64,65] Although biomass has the potential to decentralize energy production from fossil fuels, the poor yields of bioconversion processes impede these processes' large-scale industrial production. The poor yields of biofuels are mainly due to complex structures of cell walls present in the biomass, which require additional pre-treatments to efficiently break down these cell walls.[66]

To the best of our knowledge, the utilization of biomass emanating from agricultural waste for the preparation of rocket propellants has not been systematically explored yet.[67] One of the widely available agricultural products is coconut, which is produced at about 62 million tons per year.[68] Coconut husk (**CH**), which is the main agricultural waste of coconut-derived food production, contains about 42% of cellulose and 45% of lignin, making it a suitable and abundant source of biofuel.[69]

With the aim to prepare green and low-cost sustainable rocket fuels (SRFs), here we report an unprecedented approach for the conversion of **CH** into valuable "fully green" rocket propellant formulations **F1–F11**, which were shown to be hypergolic with a H_2O_2 oxidizer. A comprehensive structural characterization and thermal and energetic property evaluation of **CH**-derived fuels **NCH1–NCH4** and guanine (**GU**)-based combustion catalysts – **Mn–GU** and **Cu–GU** complexes were performed. Ignition delay studies, isothermal stability studies, and mechanistic studies to explore the nature of the ignition process of novel propellant formulations containing **Mn–GU** and **Cu–GU** complexes were also performed.

Results and discussion

Materials and methods

All commercially available reagents were used without further purification. FT-IR spectra were recorded using an ATR unit on a PerkinElmer Frontier spectrometer. Densities were measured at 25 °C by employing an Ultrapyc 1200E Quantachrome helium gas pycnometer. Elemental Analysis was performed using a Thermo Scientific Flash 2000 Organic Elemental Analyzer. DSC analyses were carried out using a PerkinElmer DSC 8000, at a heating rate of 10 °C min^{-1}. TG analyses were carried out by using a high temperature TA (SDT 650) instrument at a heating rate of 10 °C min^{-1} and under a N_2 atmosphere (flow rate: 100 mL min^{-1}). EPR measurements were performed by using a JEOL Model JES FA_{200} instrument with

an operating frequency of 9.452 GHz. SEM-EDS measurements were performed using a ZEISS Ultra-55 scanning electron microscope. The samples were subjected to gold sputtering prior to SEM-EDS measurements to prevent charging and improve image quality. The peak at 0 keV in the EDS spectra is the noise peak or strobe peak and stems from the acquisition electronics of the EDS spectrometer. XPS measurements were performed using a Thermo Scientific K-Alpha Surface Analysis using an Al Kα monochromatic excitation source of energy (1486.6 eV). The heat of combustion was measured by bomb calorimetry (Parr 6200), under O_2 pressure of 32 MPa. Solid-state UV-Vis (DRS) measurements were performed using a Shimadzu MPC3600, and UV-vis absorbance of liquid samples were measured using an Analytik Jena SPECORD S-600. Ignition tests were filmed using a Chronos (1.4) high-speed video camera operating at 2000 fps. Contact angle measurements were performed using a Rame-Hart goniometer (250-F1).

Synthesis

To convert the agricultural waste, coconut husk, into rocket fuel, we took a sample of raw coconut husk (25.0 g) from matured coconut, and washed it with water at room temperature and then with hot water to remove most of the unwanted impurities. The washed coconut husk was dried under air and ground to powder, and dry particles were sieved through a metal sieve to obtain a uniform coconut husk (**CH**) brown powder (23.0 g; Fig. 1). Subsequently, this **CH** powder (3.0 g) was slowly added to a mixture of HNO_3 and concentrated sulfuric acid (H_2SO_4) at 0 °C. At the end of the addition, the reaction mixture was stirred for 15 min, and then allowed to warm up to room temperature and kept for various periods of time (from 1 day to 4 days). Upon nitration process termination and acids dilution, the insoluble materials were collected by filtration and washed with cold water and aqueous sodium bicarbonate ($NaHCO_3$). The resulting nitrated coconut husk (**NCH1–NCH4**; Fig. 1, ESI†) yellow powders were dried under air to obtain materials that were used in all further studies. The reduction in the weights of the obtained **NCH1–NCH4** nitrated products *versus* the starting **CH** material could be explained by the degradation of most of the lignin biopolymers present in **CH** during the nitration process, where the resulting lignin-derived compounds became soluble in the nitrating mixture. The chemical compositions of **NCH1–NCH4** were comprehensively characterized by infrared spectroscopy (Fig. 3 and S3–S6; ESI†), elemental analysis (Table 1), scanning electron microscopy (SEM), and energy-dispersive X-ray spectroscopy (EDS) (Fig. 5 and 6 and S20–S23; ESI†), and UV-vis spectroscopy (Fig. 4).

Guanine (**GU**; 2-amino-1*H*-purin-6(9*H*)-one) is practically insoluble in most common organic solvents. However, it could be solubilized in acidic or basic aqueous solutions.[70] Although Fe, Ru, Pd, Pt, and Cu transition metal complexes of guanine (as a functional group of the nucleotide base of DNA or RNA) and its derivatives were described, these reports are mostly limited to the structure of complexes in which guanine is present as a neutral ligand.[71–75] The preparation of deprotonated GU transition metal complexes is highly challenging, due to the related solubility issues. In our initial attempts for the preparation of the **Mn–GU** complex, we first deprotonated this ligand by dissolving **GU** in aqueous KOH (2.0 M), which was followed by slow addition of aqueous $MnCl_2{\cdot}4H_2O$. This approach was unsuccessful due to the formation of a black Mn_3O_4 precipitate under these basic conditions, as was observed in the infrared spectroscopy analysis of this precipitate (Fig. S7; ESI†).[76] A similar problem was encountered

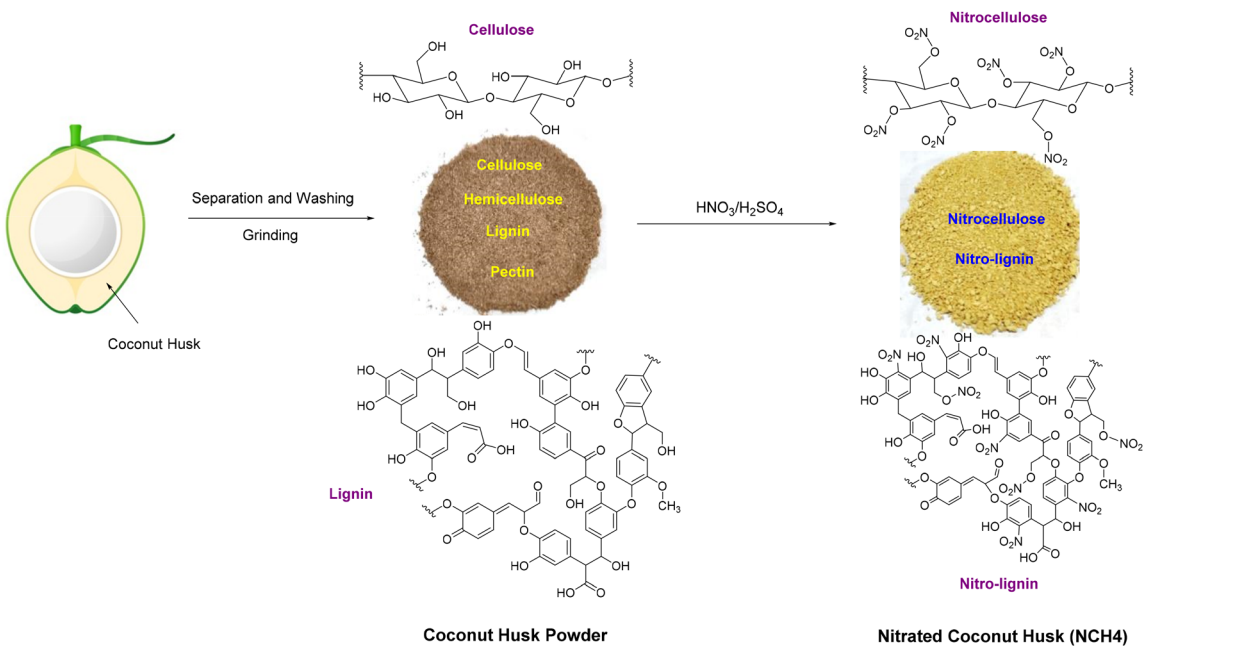

Fig. 1 Schematic of the preparation of **NCH4** fuel.

Table 1 Elemental analysis data of **CH**, **NCH1–NCH4**, **Mn–GU**, and **Cu–GU** complexes

Comp.	Formula	Carbon (C) calc./found (%)	Hydrogen (H) calc./found (%)	Nitrogen (N) calc./found (%)	C/N ratio
CH	NA	32.01/32.44	4.03/4.49	0/0	0
NCH1	$(C_{13}H_{17}N_5O_{22})_n$	26.23/26.31	2.88/2.84	11.76/11.75	2.24
NCH2	$(C_{10}H_{13}N_4O_{18})_n$	25.17/25.47	2.75/2.73	11.74/11.69	2.18
NCH3	$(C_{10}H_{13}N_4O_{17})_n$	26.04/25.78	2.84/2.84	12.15/12.22	2.11
NCH4	$(C_9H_{11}N_4O_{14})_n$	27.08/27.38	2.78/2.80	14.04/13.91	1.97
Mn–GU	$C_{10}H_{14}N_{10}MnO_5$	29.35/29.75	3.45/3.05	34.23/34.13	0.87
Cu–GU	$C_{10}H_{14}N_{10}CuO_5$	28.75/29.29	3.38/3.02	33.52/33.03	0.89

during our attempts to prepare a **Fe–GU** complex, using $FeCl_3{\cdot}6H_2O$ as a starting material. We observed that under the used basic reaction conditions, generation of iron hydroxides was preferred over the formation of **Fe–GU** complexes.

In our further efforts to counter the formation of metal oxides, we discovered that the use of a specific ratio between KOH (2.5 equivalents), **GU** (4.0 equivalents), and metal precursor salts (1.0 equivalent) prevented the preferential formation of metal oxides and directed the reaction towards the metal–**GU** complex formation. Thus, an aqueous solution of a metal precursor ($MnCl_2{\cdot}4H_2O$ or $CuCl_2{\cdot}2H_2O$) was slowly added to the basic **GU** suspension and the reaction mixture was stirred to yield the desired **Mn–Gu** and **Cu–Gu** complexes (Fig. 2 and ESI†). Notably, in contrast to the **Mn–GU** compound that was formed (in 49% yield) as an insoluble material (most probably, a coordination polymer), a **Cu–GU** complex was initially formed (in 55% yield) as a soluble compound. Upon solvent removal, during the final purification step, the **Cu–GU** complex became insoluble (forming a film), which strongly suggests its conversion into a coordination polymeric structure. The chemical structures of **Mn–Gu** and **Cu–Gu** complexes were comprehensively characterized by infrared spectroscopy (Fig. S8–S10; ESI†), elemental analysis (Table 1), SEM (Fig. 5; Fig. S20; ESI†), electron paramagnetic resonance (EPR) spectroscopy (Fig. 7), X-ray photoelectron spectroscopy (XPS; Fig. 8; Fig. S13; ESI†), solid-state UV-vis (DRS) spectroscopy (Fig. 4), and thermogravimetric (TG) analysis (Fig. 9).

FT-IR analysis

To determine the presence of different functional groups in **CH** nitration products **NCH1–NCH4**, a comparative analysis between the infrared spectra of **CH** and **NCH1–NCH4** was performed (Fig. 3 (left), Fig. S2–S6; ESI†). The spectrum of **CH** was found to fully match the previously reported spectra of coconut husk.[77] Peaks observed in the range of 1110–950 cm^{-1} in the spectrum of **CH** could be assigned to the C–O bond stretching of the glycosidic C–O–C bonds of cellulose, and hemicellulose, as well as to the phenolic C–OH and etheric C–O–C bonds present in the lignin component of **CH**.[77–79] Since the infrared spectra of compounds **NCH1–NCH4** were found to be practically indistinguishable from one another, the **NCH4** compound was used for further analysis and comparison. In

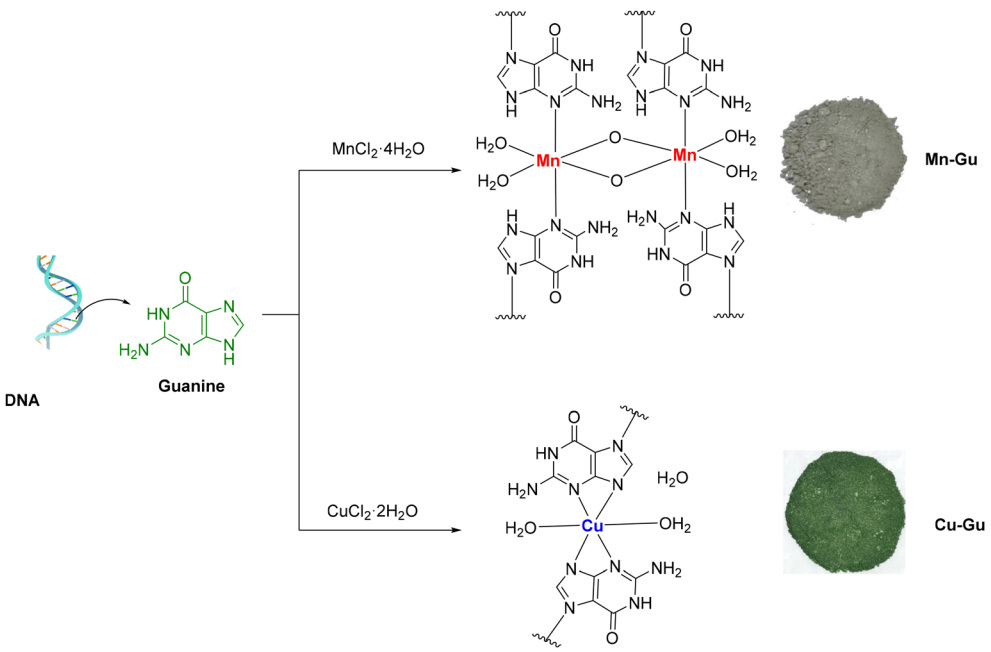

Fig. 2 Synthesis of the **Mn–Gu** and **Cu–Gu** complexes, their proposed molecular structures, and physical appearance.

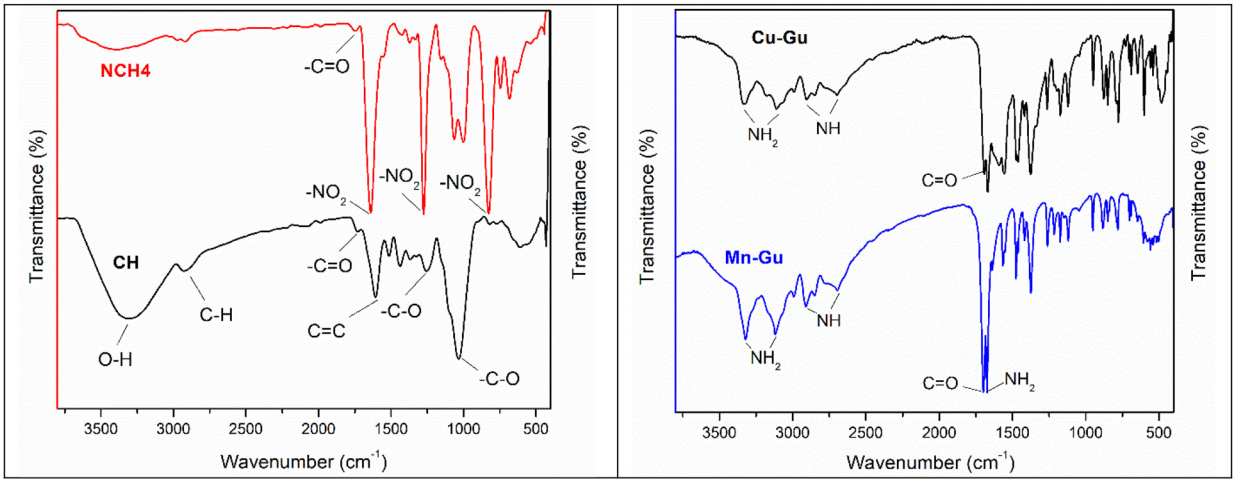

Fig. 3 FT-IR spectra. (Left): **CH** and **NCH4** and (right): **Cu–GU** and **Mn–GU** complexes.

the spectra of this compound, a significant reduction (*versus* the **CH** spectrum) in the intensity of the cellulose and hemicellulose peaks was observed at 3302 cm^{-1} (OH groups), and 2919 cm^{-1} (CH and CH_2 groups).[77–79] A reduction in the intensity of another peak at 1726 cm^{-1}, characteristic of C=O bonds in hemicellulose, pectin, lignin, and wax (all found in **CH**), showed that the nitration process of **CH** led to a significant removal of these components from the surface of the coir fibers.[76–78] An appearance of three new intense peaks in the spectrum of **NCH4** (*versus* the **CH** spectrum) at 1640 cm^{-1} (asymmetric N–O stretching), 1276 cm^{-1} (symmetric N–O stretching), and 825 cm^{-1} (O–NO_2 stretching) was a clear indication of the presence of NO_3 groups in the nitrated compounds, as a result of the conversion of OH groups in **CH** to the corresponding NO_3 groups.[80] Furthermore, in the spectrum of **NCH4**, peaks at 1606 cm^{-1} (C=C bonds of aromatic rings) and 1256 cm^{-1} (C–O stretching of acetyl groups), both belonging to lignin, present in the spectrum of parent **CH**, practically disappeared. The latter observation strongly suggests degradation of the lignin component of **CH** through the nitration process, with a subsequent dissolution and removal of resulted lignin derivatives during the nitration reaction work-up. To further confirm the degradation of lignin during the **CH** nitration, we selectively extracted lignin from **CH** (Fig. S11, ESI†),[81] and allowed to react the extracted lignin with a mixture of HNO_3 and H_2SO_4 for 4 days. After completion of the reaction, about 97.0 wt% of the lignin was found to be soluble in the nitration reaction mixture, indicating this bio-polymer fragmentation into smaller molecules and/or acid-soluble products. The infrared spectral analysis clearly indicates that the prepared **NCH1–NCH4** materials are mostly composed of nitrocellulose,[80] along with some small amounts of nitro-lignin derivatives trapped in it.

The infrared spectra of **Mn–GU** and **Cu–GU** complexes showed similar patterns to the spectrum of the parent **GU** ligand, in the range of 2500–3500 cm^{-1}, corresponding to the NH_2 and NH groups of **GU** (Fig. 3 (right), Fig. S8–S10; ESI†). The peaks at 1691 cm^{-1} (C=O) and 1668 cm^{-1} (NH_2 scissoring) did not show any significant shift *versus* the parent **GU**,[82] indicating that both NH_2 and C=O groups of **GU** did not have any significant interaction with the metal centers in **Mn–GU** and **Cu–GU** complexes. In the case of the **Cu–GU** complex, appearance of new peaks at 1591 cm^{-1} (C=C bond) and 1555 cm^{-1} (C=N bond) was observed, while peaks at 1635 cm^{-1} and 1563 cm^{-1}, belonging to the vibrations of the same bonds in the parent **GU**, disappeared.[82] This significant change (shift) could be explained by the binding of the **GU** ligand in its deprotonated form, *via* its N7 and/or N9 nitrogens, to the Cu metal center in the **Cu–GU** complex. In contrast, in the infrared spectrum of the **Mn–GU** complex, the intensity of 1635 cm^{-1} and 1563 cm^{-1} peaks was only reduced, and no shifts due to **GU** complexation with the Mn metal center *via* its N7 and/or N3 nitrogens were observed. These results clearly indicate the difference in the **GU** ligand binding modes in the **Mn–GU** and **Cu–GU** complexes and different molecular structures of these complexes. In the fingerprint region (1000–500 cm^{-1}), in the spectra of both **Mn–GU** and **Cu–GU** complexes, significant changes in the peak pattern and intensity (*versus* the parent **GU**) were observed, indicating that heterocyclic rings of the **GU** ligand had participated in the metal center coordination.

Elemental analysis

The elemental composition of **NCH1–NCH4**, **Cu–GU** and **Mn–GU** complexes was obtained from elemental analysis (CHN) measurements (Table 1). Since the main components of the dried coconut husk were cellulose, lignin, and hemicellulose, no nitrogen-containing molecules should be present in **CH**.[69] Indeed, our analysis of the **CH** samples showed only the presence of carbon (32.44 wt%) and hydrogen (4.49 wt%); the rest were oxygen atoms. In comparison with **CH**, samples of **NCH1–NCH4** showed significantly lower carbon and hydrogen content. This observation could be the result of lignin and hemicellulose removal from **CH** upon its nitration. Another

important observation was found in **NCH1–NCH4** materials, where their nitrogen content increased from 11.75 wt% in **NCH1** (product of nitration for 24 h) to 13.91 wt% in **NCH4** (product of nitration for 96 h), indicating that the longer nitration time led to a higher number of NO_3 groups. These results were further supported by carbon-to-nitrogen (C/N) ratios calculated for the **NCH1–NCH4** material, which were showing a gradual decrease as the nitrogen content in the material was increased due to the prolonged nitration time (Table 1). Empirical formulas derived from the elemental analyses of the **NCH1–NCH4** material are presented in Table 1. The empirical formula calculated for the **Mn–GU** and **Cu–GU** complexes indicates the presence of two **GU** ligands per each Mn and Cu metal centers, respectively (Table 1).

UV-vis spectroscopy studies

The UV-vis spectrum of **NCH4** (1.0 mg mL^{-1} in DMSO) showed a peak at 252 nm, adjacent to a broad peak/plateau (between 314 and 453 nm) with a small maximum at 373 nm (Fig. 4 (left)), where the spectrum of coconut husk-extracted lignin (1.0 mg mL^{-1} in DMSO) also showed a peak at 252 nm, adjacent to even broader plateau (between 314 and 537 nm) (Fig. 8 (left)). A comparison between the spectra of **NCH4** and lignin in the 200–300 nm region indicated the presence of phenolic moieties in both materials.[83] The appearance of the new peak at 373 nm and disappearance of peak at 537 nm in **NCH4** indicated that the lignin present in **NCH4** probably undergoes nitration to form nitro-lignin.

To assess the concentration of nitro-lignin in **NCH4**, we selectively extracted the nitro-lignin from **NCH4** using a similar procedure previously reported for lignin extraction from cellulose–lignin mixtures (ESI†).[81] We were able to extract 0.3 wt% of nitro-lignin from **NCH4**. The FT-IR analysis of the extracted nitro-lignin showed peaks at 1631 cm^{-1} that correspond to nitro groups, confirming the formation of nitro-lignin (Fig. S12; ESI†). Therefore, a small and broad peak at 373 nm in the UV-vis spectrum of **NCH4** could be attributed to the formed nitro-lignin.[84] Such a low content of nitro-lignin in the **NCH4** material could be attributed to degradation of lignin during the nitration process.

Due to a lack of solubility of polymeric **Mn–GU** and **Cu–GU** complexes in common solvents, solid-state UV-vis (diffuse reflectance spectroscopy, DRS) analysis of these complexes was performed (Fig. 4 (right)). Using the Kubelka–Munk function, $F(R_\alpha)$ (eqn (1)), the measured reflectance spectra were converted into absorption spectra as shown in Fig. 4 (right).[85]

$$F(R_\alpha) = \frac{K}{S} = \frac{(1 - R_\alpha)^2}{2R_\alpha} \quad (1)$$

where $R_\alpha = R_{sample}/R_{standard}$, and K and S are the absorption and scattering coefficients, respectively.

The UV-vis DRS spectrum of solid **GU** showed two broad peaks with absorption maxima (λ_{max}) of 244 and 276 nm. These peaks could be assigned to the $\pi \rightarrow \pi^*$ transition of **GU**.[82] Upon the formation of **Mn–GU** and **Cu–GU** complexes, only a slight change in the λ_{max} of these peaks was observed. While three new peaks appeared for both **Mn–GU** and **Cu–GU** complexes with a λ_{max} of 378, 480 and 512 nm (for **Mn–GU**), and 378, 482, and 522 nm (for **Cu–GU**). These peaks in the range of 375–540 nm could be assigned to metal-to-ligand charge transfer (MLCT) transitions, further proving the successful formation of metal–**GU** complexes.[82]

Scanning electron microscopy–energy dispersive X-ray spectroscopy studies

The sizes and shapes of solid fuel particles, as well as the presence of cracks, pores and voids in composite propellants may affect these propellants' performance.[86] We used SEM equipped with EDS to study the morphology of **CH** and **NCH1–NCH4** materials (Fig. 5 and Fig. S20; ESI†). The SEM images of the **CH** surface revealed its superimposed lamellar-shaped structure, with a number of cracks and defects and the presence of some small particulate impurities. The irregular distri-

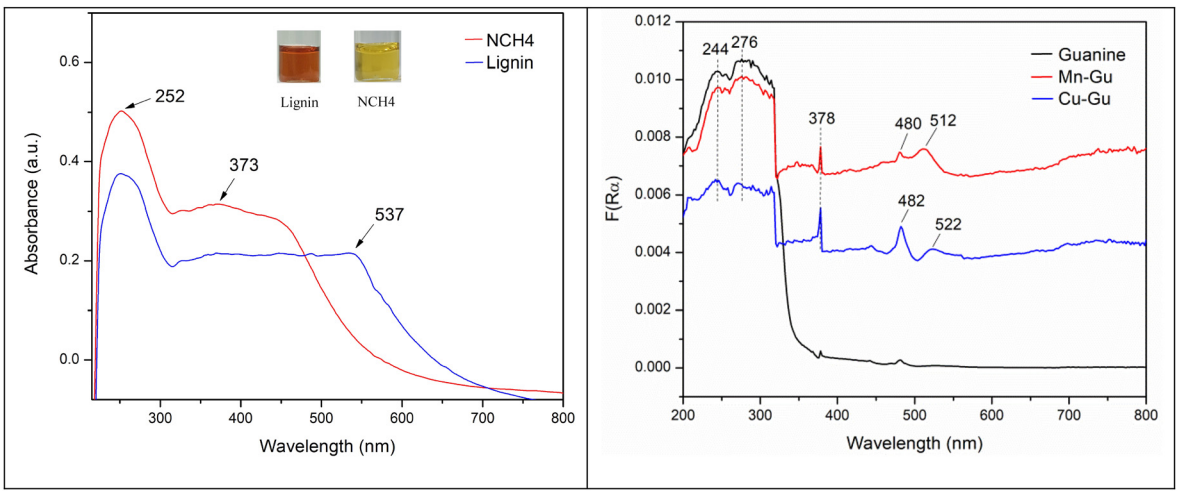

Fig. 4 (Left): UV-vis spectra (baseline subtracted) of **NCH4** and lignin in DMSO; (right): solid state UV-vis (DRS) spectra of **GU**, **Mn–GU**, and **Cu–GU**.

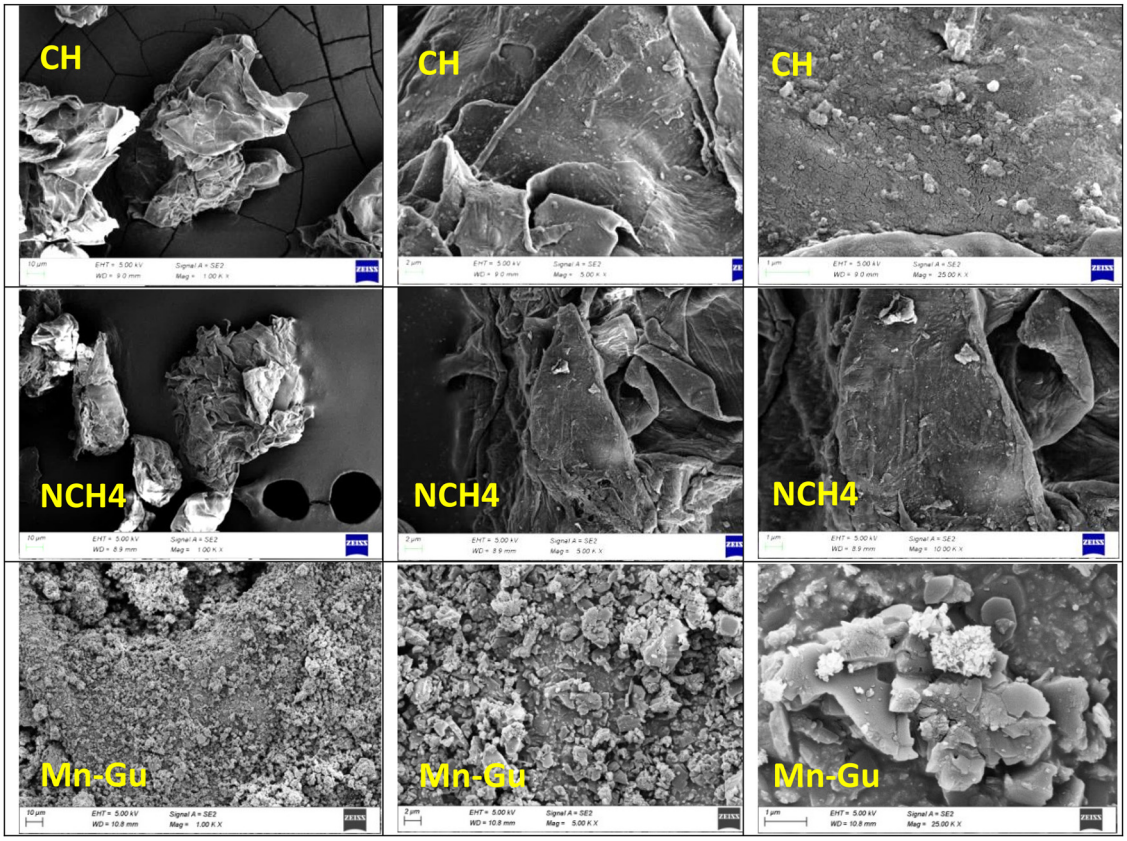

Fig. 5 SEM images. (Top): **CH**; (middle): **NCH4**; (bottom): **Mn–GU** complex.

bution of fats, wax and other materials (including impurities) represented a non-uniform structure of **CH**. Upon nitration of **CH**, the surface roughness of the produced **NCH1–NCH4** materials became smoother and flatter, with a much lower number of defects on it. The smoothness of the **NCH1–NCH4** material surface could be the result of efficient removal of surface-adhered impurities, as well as of wax and fatty acids. It was found that with the prolongation of the time of nitration, the smoothness of the surface changed. The longer nitration time and the higher degree of nitration led to smoother surfaces in the **NCH1–NCH4** materials (Fig. S20; ESI†), which is probably the result of better removal of hemicellulose and lignin, along with wax and fats from **CH**.

EDS analyses were also performed to identify the elements present in both **CH** and **NCH1–NCH4** materials. Only carbon and oxygen were found for **CH**, while samples of **NCH1–NCH4** showed the presence of carbon, nitrogen, and oxygen (Fig. 6 and Fig. S21–S23; Tables S1–S4; ESI†). The obtained C/N ratios

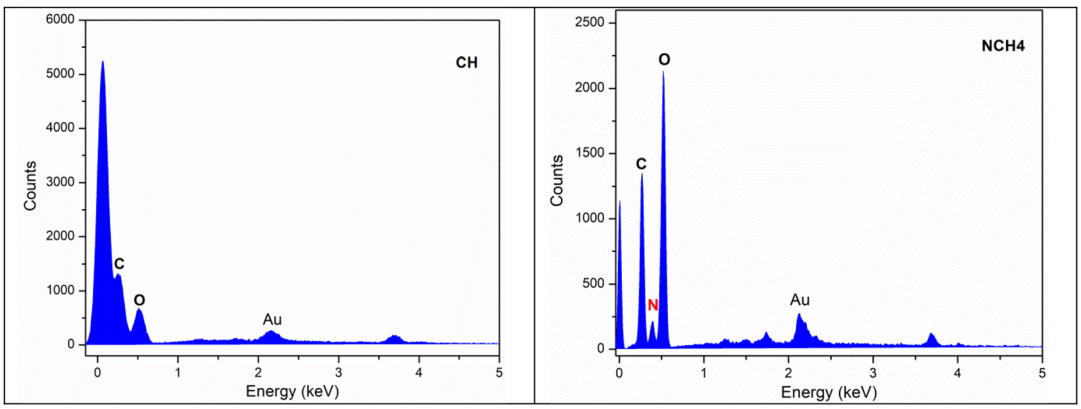

Fig. 6 Representative EDS spectra. (Left): **CH**; (right): **NCH4**.

(wt%) for **NCH1–NCH4** were found to be in good agreement with the C/N ratios that were obtained from the elemental analysis of these materials (Table 1). SEM analysis of **Mn–GU** and **Cu–GU** complexes revealed that their surfaces had amorphous structures.

Electron paramagnetic resonance studies

X-band electron paramagnetic resonance (EPR) spectrometry measurements (at room temperature) of both **Mn–GU** and **Cu–GU** complexes (in the solid state) were performed to study the oxidation states of the metal centers and their molecular geometry. The EPR spectrum of **Mn–GU** showed a broad signal with a g value of 1.98 (Fig. 7, left). This observation indicates the presence of the Mn(II) metal center in the **Mn–GU** complex.[87] The absence of fine or hyperfine splitting also suggests that upon coordination of the Mn(II) metal center with the **GU** ligand, the symmetry around the Mn(II) center became distorted. Due to this distorted symmetry, the resonances become anisotropic, leading to a broad line. The presence of the broad lines in the EPR spectrum of the **Mn–GU** complex may indicate a polymeric nature of this complex.[88] The analysis of the EPR spectrum of the **Cu–GU** complex showed a typical pattern of the Cu(II) metal center, with $g_{\parallel}$ and $g_{\perp}$ values of 2.28 and 2.06, respectively, and a g_{av} of 2.13 (Fig. 7, right).[89] The deviation of g_{av} of the **Cu–GU** complex from the free electron (2.0023) was due to the coordination of the Cu(II) metal center with the **GU** ligand. In the case of the latter complex, the following trend for $g_{\parallel}$ and $g_{\perp}$ values was observed – $g_{\parallel} > g_{\perp} > 2.0023$ – which is characteristic of the axial symmetry of Cu(II) complexes.[89]

X-ray photoelectron spectroscopy studies

A single crystal X-ray crystallography analysis of both **Mn–GU** and **Cu–GU** complexes could not be obtained due to the lack of solubility of these complexes in water and all evaluated organic solvents. Both the X-ray powder diffraction and SEM analyses showed that these complexes are amorphous in their nature. Therefore, X-ray photoelectron spectroscopy (XPS) analyses were used to obtain information regarding the **Mn–GU** and **Cu–GU** structures and the metal–**GU** bonding arrangements. The XPS spectra (survey) of **Mn–GU** showed the presence of Mn, C, N, and O elements in this complex structure (Fig. 8, top left). The deconvoluted high-resolution spectra of Mn 2p showed two main peaks at 641.88 and 653.68 eV, corresponding to Mn $2p_{3/2}$ and Mn $2p_{1/2}$, respectively (Fig. 8, top middle).[90] The energy difference between the Mn $2p_{3/2}$ and Mn $2p_{1/2}$ states was found to be 11.8 eV. This energy difference strongly suggested the presence of Mn(II) metal center.[90] A satellite peak was also observed at 643.48 eV, which was characteristic of the Mn(II)–O bond.[91] In the case of the C 1s spectrum of **Mn–GU**, three peaks at 284.99, 286.40, and 288.05 eV were observed (Fig. S13a, ESI†). The peak at 284.99 eV could be assigned to the C–C and C–H bonds of **GU**. The other peaks at 286.40 eV corresponded to the C–N–C and N–C–N bonds, while the peak at 288.05 eV corresponded to the N–C=O bonds of **GU**. The N 1s spectrum showed two peaks at 398.84 and 400.24 eV, which could be assigned to the N=C and NH_2–C bonds of **GU**, respectively (Fig. S13b, ESI†).[92] In terms of its spectral pattern and binding energy, both the C 1s and N 1s spectra of **Mn–GU** were found to be different from the pure **GU** spectrum. This observation further confirmed the coordination of the Mn center with the N-ring atoms of **GU**.[93] The deconvoluted spectrum of O 1s showed three peaks, where the peak at 529.68 eV could be assigned to the oxo-bridged Mn–O–Mn bonds (Fig. 8, top right).[94] The other two peaks at 531.26 and 531.8 eV corresponded to the C=O bonds of **GU** and water molecules, present in the structure of the **Mn–GU** complex, respectively.

The XPS spectra (survey) of **Cu–GU** showed the presence of Cu, C, N, and O in its structure (Fig. 8, bottom left). The deconvoluted spectra of Cu 2p showed two major peaks at 932.85 and 952.63 eV, corresponding to the Cu $2p_{3/2}$ and Cu $2p_{1/2}$ states of Cu(II), respectively (Fig. 8, bottom middle).[95,96] Similar to **Mn–GU**, the C 1s spectrum of **Cu–GU** also showed three peaks at 287.86, 286.28 and 285.2; the N 1s spectrum showed two peaks at 400.15 and 398.8 eV and the O 1s spectrum showed two peaks at 531.48 and 531.15 eV (Fig. 8,

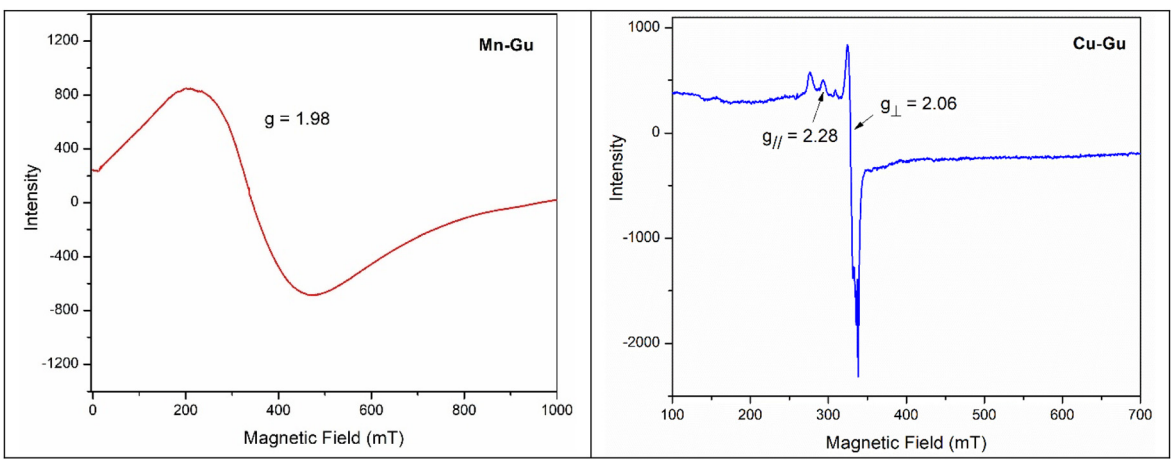

Fig. 7 EPR spectra of powdered **Mn–GU** and **Cu–GU** complexes.

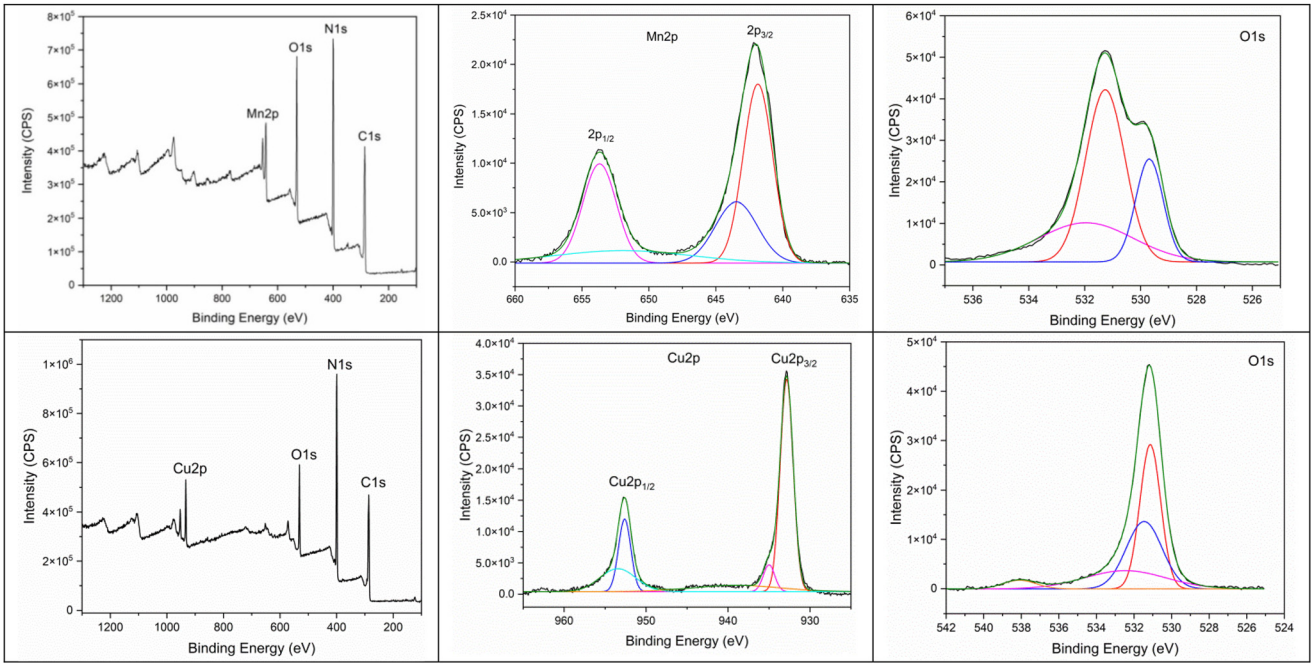

Fig. 8 XPS spectra of **Mn–GU** (top) and **Cu–GU** (bottom) complexes.

bottom right, and Fig. S13c and S13d, ESI†). The shape of the N 1s and C 1s spectra of **Cu–GU** were found to be different from the spectra of **Mn–GU** and **GU**, and the binding energies were also found to be different. This could be the effect of the different binding modes of **GU** to Cu, where the NH ring proton of **GU** was probably deprotonated by KOH. While, in the case of **Mn–GU**, no deprotonation occurred, and **GU** bound to the Mn center as a neutral ligand.

Study of thermal and energetic properties

To study the thermal properties of **NCH1–NCH4** fuels and **Mn–GU** and **Cu–GU** complexes, differential scanning calorimetry (DSC) and thermogravimetric (TG) analyses were performed. The TG thermogram of the **Mn–GU** complex showed that this material was highly thermostable, with its peak decomposition temperature at about 500 °C (Fig. 9, left). Decomposition occurred in two continuous steps, leading to 82% mass loss of the sample. Upon heating, the sample of **Mn–GU** lost its coordinatively bound water molecules, well above 100 °C. This dehydration process resulted in 16.8% (observed experimentally) mass loss of the samples, which corresponded to four molecules of water, loss of which should lead to a calculated weight reduction of 17.12%. Our predicted structure of **Mn–GU**, where two water molecules were coordinatively bound to each Mn metal center, was in line with these TGA results (Fig. 2). It was reported that high temperature (about 800 °C) decomposition under an inert atmosphere of oxygen/water-containing Mn complexes typically produces MnO as the final product.[97] Considering the formation of MnO residue in the case of **Mn–GU** thermal degradation, 17.34% (calculated) of mass should remain after the TG analysis of this complex. This calculated value of the MnO residue was found to be in accordance with our experimental TG results (observed 18% residue), further confirming the proposed chemical composition of the **Mn–GU** complex.

In contrast to **Mn–GU**, the TG thermogram of **Cu–GU** showed a two-stage decomposition process (Fig. 9, right). The two-step decomposition process could be due to the presence of the deprotonated **GU** ligand in the **Cu–GU** complex. The first-stage decomposition showed a mass loss of 27.51%, with a peak temperature of 458 °C, while most of the mass was lost in the second stage (45.99%), with a peak temperature of 660 °C. The residual mass could be attributed to the formation of copper oxides (CuO or Cu_2O).

The DSC thermograms of **NCH1–NCH4** showed a similar decomposition pattern, with the peak decomposition temperature of about 207 °C (Fig. 10). Although these decomposition patterns were similar, the total amount of energy released was found to vary from 1574 J g^{-1} for **NCH1** to 1544 J g^{-1} for **NCH4** (Fig. S14–S17; ESI†). This small change in energy release could be the effect of variation in the degree of nitration and percentage of nitro-lignin present in each sample. To further evaluate the energetic properties of **NCH1–NCH4** materials, bomb calorimetry analyses under an O_2 atmosphere were performed. These analyses showed that upon removal of lignin, hemicellulose and other impurities, during the nitration process, the heat release of **NCH4** was reduced to almost half of the untreated **CH** (Table 2). Due to the differences in the structure, the total heat release of the **Mn–GU** complex was found to be slightly higher than that of **Cu–GU**.

From the heat release data obtained by bomb calorimetry analyses, the enthalpies of formation of **NCH4**, **Mn–GU**, and

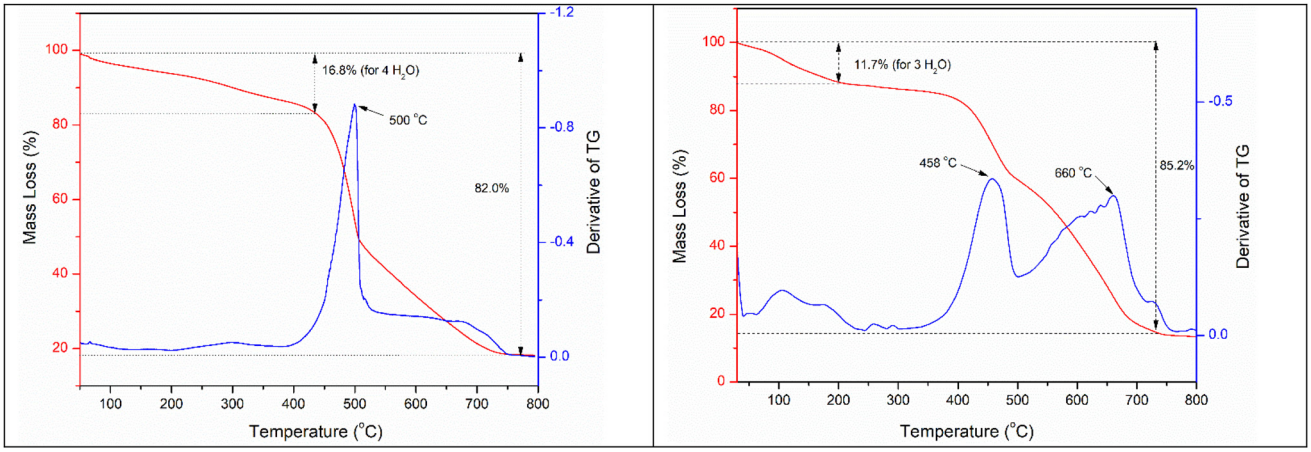

Fig. 9 (Left): TGA thermograms of the **Mn–GU** complex; (right): TGA thermograms of the **Cu–GU** complex.

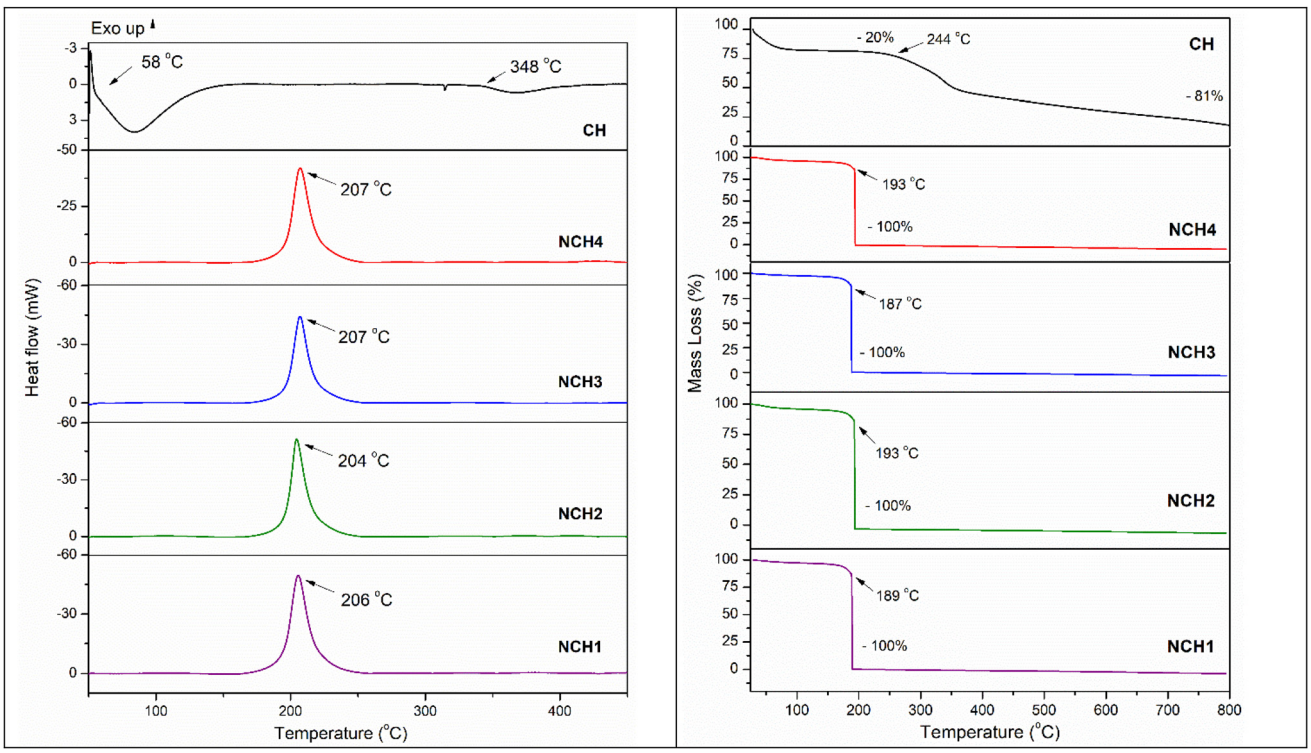

Fig. 10 (Left): DSC thermograms of **CH** and **NCH1–NCH4** materials; (right): TGA thermograms of **CH** and **NCH1–NCH4**.

Cu–GU were calculated (Table 2 and ESI†). The heat release of the formulations **F1** and **F8** was found to be 1442 and 1444 J g^{-1}, respectively (Fig. S18 and S19; ESI†). The reduction in heat release (by 100 J g^{-1}) than that of **NCH4** was due to the presence of non-energetic **Mn–GU** and **Cu–GU** complexes.

Ignition studies with hydrogen peroxide

After comprehensive structural characterization and thermal and energetic property evaluation of the prepared materials, their ignition tests were performed using high grade H_2O_2 (95%) to show their potential application as hypergolic fuels in hybrid rocket engines. All the ignition events were recorded using a high-speed video camera, operating at 2000 frames per second (fps). For these tests, powdered samples (about 30 mg) were placed in a white transparent glass vial and one drop of H_2O_2 (15 μL) was added. The time difference between the initial contact of oxidizer droplet with the surface of the material,

Table 2 Physical and energetic properties of CH, NCH4, Mn–GU and Cu–GU complexes

Materials	Density (g cm^{-3})	T_p (°C)	Energy density (MJ kg^{-1})	ΔH_c (kJ mol^{-1})	ΔH_f (kJ mol^{-1})
CH	1.23	367	17.82	NA	NA
NCH4	1.38	207	8.64	−3433.6	−1680.06
Mn–GU	1.80	500	10.01	−4088.96	−2106.95
Cu–GU	1.74	458	9.34	−3893.83	−2066.65

until the appearance of a clearly visible flame was determined as an ignition delay (ID) time. An ID time below 50 ms is crucial for proper functioning of hypergolic propulsion systems.[14]

Although both the **Mn–GU** and **Cu–GU** complexes were found to be highly reactive with H_2O_2, no clearly visible flame was observed during the addition of H_2O_2 (95%) to the compounds (Fig. S24†). The high decomposition temperature of both **Mn–GU** and **Cu–GU** and the absence of energetic functional groups in their structure could be the main reason for lack of any visible flames' appearance.

Thereafter, we prepared formulations of **Mn–GU** (promoter) and **NCH1–NCH4** (fuels) at a promoter-to-fuel ratio of 25 : 75 wt%, by grinding both the materials together using a mortar and pestle. The SEM analysis of **F1** formulation showed a homogeneous distribution of **Mn–GU** particles over the surface of the **NCH4** fuel (Table 3; Fig. S20; ESI†). The prepared **Mn–GU**-based (25 wt%) formulations of **NCH1–NCH4** (**F2**, **F5**, **F6** and **F7**; ESI†) were found to exhibit fast hypergolic ignitions with H_2O_2 (95%), showing ID times below 50 ms, where **F2** showed the lowest ID time of 42 ms (Table 3, Fig. 11, and S24; ESI†). Among these formulations, the shortest ID time for **F2** could be attributed to the higher degree of nitration of **NCH4** in comparison with **NCH1–NCH3**.

To study the influence of **Mn–GU** content on ID time, three additional formulations, namely, **F1**, **F3**, and **F4**, were prepared (Table 3). The formulation **F1**, with the highest **Mn–Gu** content, showed the lowest ID time of 36 ms, while the formulations **F3** and **F4** showed ID time of 47 and 49 ms, respectively. The ID time of 49 ms for **F4** formulation was highly impressive, as it contained only 2 wt% of Mn metal in its composition, making it very promising for application as a hypergolic fuel in hybrid rocket motors.

In the case of **Cu–GU** formulations **F8** and **F9**, comparatively higher ID times of 159 and 158 ms were observed. The longer ID times observed for **Cu–GU** formulations (**F8** and **F9**) *versus* similarly composed **Mn–GU** formulations (**F1** and **F2**) could be explained by a lower reactivity of the **Cu–GU** complex with H_2O_2, in comparison with **Mn–GU**. To further demonstrate the potential application of **NCH4** as a hypergolic fuel, it was mixed with Janus-type H_2O_2 ignitophore (**JN14** and **JN15**) and $[FcCH_2N(Me)_3][I]$, previously reported by us.[54] The formulations **F10** and **F11** exhibited impressive ID times of 19 and 38 ms with H_2O_2 (95%), respectively (Fig. S24; ESI†). However, in the case of formulations **F20–F22**, ID times above 100 ms were observed (Fig. S24; ESI†). This showed that as per operational requirements, the **NCH4** fuel could be mixed with any suitable ignitophores, to tune and obtain the desired ignition delay time. To further demonstrate the ignition capability of our prepared materials under an inert atmosphere, we performed an ignition test of formulation **F11** under an N_2 atmosphere (Fig. S25; ESI†). Under the N_2 atmospheric conditions, **F11** showed an ID time of 40 ms, which was similar to the ID time under open-air conditions.

We observed an orange-coloured flame in most of the formulations during their hypergolic ignition with H_2O_2. Only $CuCl_2{\cdot}2H_2O$ containing formulation **F18** showed a greenish coloured flame. Thereafter, we studied the flame propagation of formulation **F4** with time. Soon after the appearance of a clearly visible flame at 49 ms, the flame continued to grow at a very fast rate, reaching a maximum height of about 9.3 cm within 6 ms (Fig. S26, ESI†). After 75 ms, the flame started decreasing gradually, and the process continued to 202 ms, until the flame disappeared. For **F1–F4**, an ignition duration of about 200 ms was observed, while for **F10–F11**, a relatively longer duration of about 300 ms was observed.

Table 3 Summary of ID times, specific impulses, and density specific impulses for Mn–GU and Cu–GU complexes and F1–F11 formulations with an H_2O_2 oxidizer (NI = no observed ignition)

	Fuel name	Composition	ID time (ms)	Specific impulse (I_{sp}; s)	Oxidizer-to-fuel ratio (O/F)	Density specific impulse (ρI_{sp}; s g cm^{-3})
1	**Mn–GU**	—	NI	228	2.00	347
2	**Cu–GU**	—	NI	223	2.00	341
3	**F1**	**NCH4** (70 wt%) + **Mn–GU** (30 wt%)	36	237	1.25	341
4	**F2**	**NCH4** (75 wt%) + **Mn–GU** (25 wt%)	42	238	1.15	343
5	**F3**	**NCH4** (80 wt%) + **Mn–GU** (20 wt%)	47	239	1.10	342
6	**F4**	**NCH4** (85 wt%) + **Mn–GU** (15 wt%)	49	240	1.00	341
7	**F8**	**NCH4** (70 wt%) + **Cu–GU** (30 wt%)	159	236	1.15	340
8	**F9**	**NCH4** (75 wt%) + **Cu–GU** (25 wt%)	158	237	1.10	339
9	**F10**	**NCH4** (75 wt%) + **JN15** (25 wt%)	19	251	1.50	354
10	**F11**	**NCH4** (85 wt%) + **JN15** (15 wt%)	38	248	1.20	350

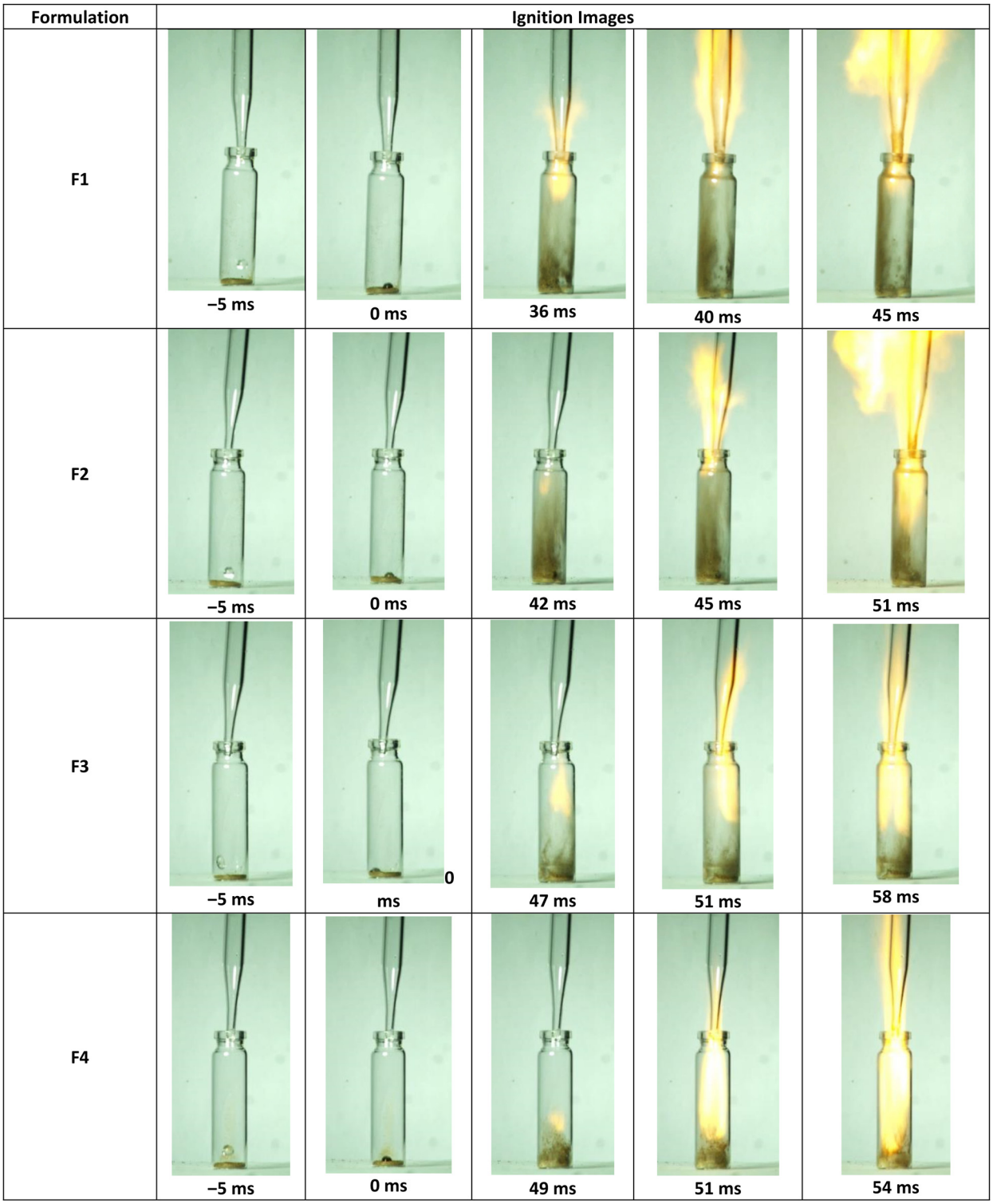

Fig. 11 Hypergolic ignition images of **F1–F4** formulations with H_2O_2 (95%). The ID values reported are an average of three experiments.

Specific impulse calculations

Specific impulse is one of the most important properties of a propellant, which determines the efficiency of a rocket motor in generating thrust. For solid propellants, a specific impulse close to 250 s is highly desired.[98] The specific impulses of **Mn–GU**, **Cu–GU**, and their formulations **F1–F4**, and **F8–F9**, as well as for **JN15**-based formulations **F10** and **F11** were calculated

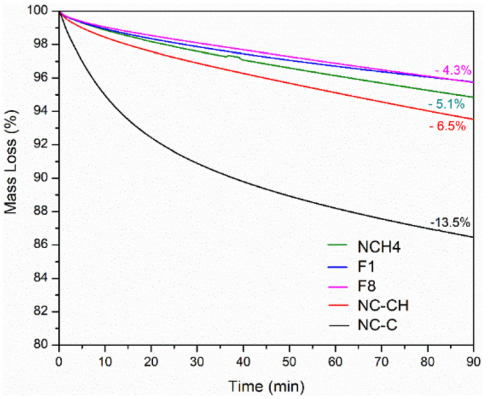

Fig. 12 TGA thermograms of **NCH4**, **F1**, **F8**, **NC–CH**, and **NC–COT** materials.

using EXPLO 5 (V 6.04) software (Table 3 and Fig. S27–S36; ESI†). Both **Mn–GU** and **Cu–GU** showed lower specific impulses of 228 and 223 s, while their formulations **F1–F4**, **F8** and **F9** showed higher specific impulses in the range of 236–240 s. In the case of formulation **F10**, a maximum specific impulse of 251 s was observed. The specific impulse curves showed a parabolic pattern, and the maximum specific impulse was observed when the O/F ratio was either 1 or slightly above 1 (Fig. S27–S36; ESI†). The density specific impulse of formulations **F1–F4** was calculated to be in the range of 341–343 s g cm^{-3}. Similar to the specific impulse (I_{sp}) of the **F10** formulation, its density specific impulse (ρI_{sp}) was also found to be higher (ρI_{sp} = 354 s g cm^{-3}) than other prepared formulations. The specific impulse of **F4** and **F10** was further calculated with liquid oxygen (LOx), and the results were found to be slightly higher than that obtained for H_2O_2 (95%) (Fig. S37 and S38; ESI†). ID time and I_{sp} and ρI_{sp} values showed that formulations **F4**, **F10**, and **F11** have the potential to be used as high-performing hypergolic fuels.

Stability studies

An important criterion of an efficient propellant is to have good chemical and thermal stability under prolonged storage conditions.[99] To evaluate the potential use of various materials prepared in this study, as prospective propellants, isothermal TG measurements were performed. In these analyses, the mass loss of **NCH4**, **NC–CH** (Fig. 12), **NC–COT** (nitrocellulose obtained from cotton), and **F1** and **F8** formulations were monitored for 90 min, at a constant temperature of 145 °C, which was 5 °C below the auto-ignition temperature of **NC–COT** (150 °C) (Fig. 12).[100] In the case of **NCH4**, only 5.1% mass loss was observed, in comparison with **NC–COT** (mass loss of 13.5%). The higher stability of **NCH4** could be attributed to the presence of nitro-lignin in this material. **NC–CH** also showed a mass loss of 6.5%, which was also significantly lower than that of **NC–COT**. This result could be explained by incomplete removal of lignin during the extraction of cellulose from **CH**.[100] Similarly, the best performing hypergolic formulation **F1** exhibited excellent thermostability in our TG analyses, with mass loss of just 4.3%. Apart from nitro-lignin, the presence of amino groups (from **GU**) in highly thermostable metal complexes **Mn–GU** and **Cu–GU** can trap the formed nitroxyl or NO_x radicals, during the decomposition of nitrocellulose, thus improving chemical and thermal stabilities of **F1** and **F8** formulations under elevated temperature conditions.

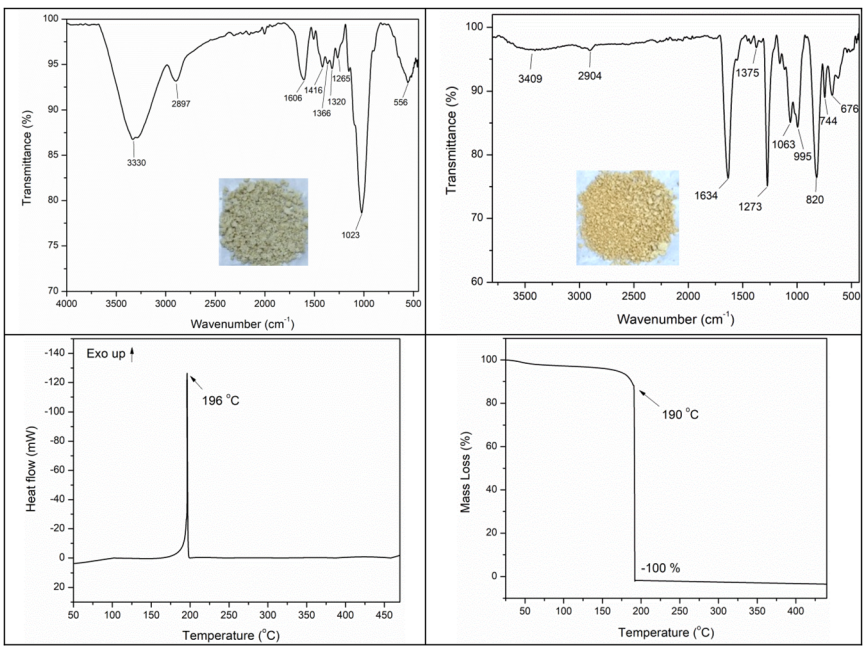

Fig. 13 FT-IR spectra and the image of the materials. (Top left): **CH**-extracted cellulose; (top right): **NC–CH**. (Bottom left): DSC thermogram of **NC–CH**; (bottom right): TGA thermogram of **NC–CH**.

Mechanistic studies

The characterization of the **NCH4** composition showed that this material mainly comprises nitrocellulose and a small amount of nitro-lignin. Since **Mn–GU**, **Cu–GU**, and their formulations with **CH** did not show any hypergolic ignitions with H_2O_2 (95%), the nitrocellulose presence in **NCH4** could be the main reason for the successful hypergolic ignitions of formulations **F1–F9** with H_2O_2 (Table 3, Fig. 11 and S24; ESI†). To validate this hypothesis, we extracted cellulose from **CH** and nitrated it to prepare nitrocellulose (**NC–CH**; ESI†). Extraction of cellulose from **CH** was performed in two steps, which included delignification, followed by a bleaching process (ESI†). The infrared spectrum of the **CH**-extracted cellulose matched the reported spectra of the cellulose obtained from other resources, such as cotton, wood, and bacteria (Fig. 13, top left).[101] The infrared spectrum, DSC and TGA thermograms, and the elemental analysis of the **NC–CH** material [N (12.07 wt%), C (25.92 wt%) and H (2.73 wt%)] revealed its chemical composition (Fig. 13).

Table 4 Ignition test of various formulations of **CH**, **NC–CH** and **NCH4** materials with H_2O_2 (NI = no observed ignition; NR = no observed reaction)

Sl. no.	Fuel name	Composition	ID time (ms)
1	**F12**	**NC–CH** (75 wt%) + **Mn–GU** (25 wt%)	40
2	**F13**	**NCH4** (75 wt%) + **GU** (25 wt%)	NR
3	**F14**	**CH** (75 wt%) + **Mn–GU** (25 wt%)	NI
4	**F15**	**CH** (75 wt%) + **Cu–GU** (25 wt%)	NI
5	**F16**	**NCH4** (75 wt%) + **$MnCl_2{\cdot}2H_2O$** (25 wt%)	NI
6	**F17**	**NCH4** (75 wt%) + **MnO_2** (25 wt%)	733
7	**F18**	**NCH4** (75 wt%) + **$CuCl_2{\cdot}2H_2O$** (25 wt%)	510
8	**F19**	**NC–CH** (85 wt%) + **JN15** (15 wt%)	26
9	**F20**	**NCH4** (85 wt%) + **JN14** (15 wt%)	115
10	**F21**	**NCH4** (85 wt%) + **[$FcCH_2N(Me_3)$][I]** (15 wt%)	278
11	**F22**	**NCH4** (90 wt%) + **JN15** (10 wt%)	162
12	**F23**	**NL** (85 wt%) + **Mn–GU** (15 wt%)	NI

Thereafter, we prepared formulations **F12–F19** and evaluated their capability to show hypergolic ignition with H_2O_2 (95%). Among these formulations, **F12** exhibited the ID time (40 ms), which was even slightly shorter than that of formulation **F2** (Table 4 and Fig. S24; ESI†). This ID time of **F12** could be explained by an absence or very low content of nitro-lignin in **NC–CH**. Similarly, **F19** also exhibited an ID time of 26 ms, which was 12 ms shorter than formulation **F11**. This observation and the lack of **Mn–GU** and **Cu–GU** ignitability with H_2O_2 proved that nitrocellulose present in **NCH1–NCH4** (and the corresponding **F1–F9** formulations) was the critical component responsible for the hypergolic ignition of these fuels. However, for the nitro-lignin (NL) formulation **F23**, no ignition was observed.

To further study the importance of metal–ligand cooperativity (MLC) on ID time, ignition tests with the precursors of **Mn–GU** and **Cu–GU** were performed (Table 4). The $MnCl_2{\cdot}2H_2O$-containing formulation **F16** exhibited only a slow decomposition of H_2O_2 without any flame appearance. In contrast, MnO_2-containing formulation **F17** and $CuCl_2{\cdot}2H_2O$-containing formulation **F18** showed slow hypergolic ignitions, with ID times of 733 ms and 510 ms, respectively, showing a critical role of the MLC on the catalysed ignition processes. The metal (**Mn** and **Cu**) and **GU** ligand MLC is involved in the decomposition of H_2O_2 to generate active radical or anionic species ($^{\bullet}OH$ or HOO^{-}), which reacts with nitrocellulose. These exothermic reactions generate sufficient amounts of heat to initiate the ignition process.[55,102] The DSC analyses of formulations **F1** and **F8** showed a single stage decomposition process with a peak temperature at about 205 °C, which is close to the decomposition temperature of **NCH4** (Fig. 14 and S18 and S19; ESI†). It means that the synergistic effect of the exothermic decomposition of **NCH4** also leads to the decomposition of **Mn–GU** and **Cu–GU** complexes at a much lower temperature than their individual decomposition temperatures.

The ID time of a hypergolic solid fuel not only depends on the chemical composition of this fuel, but also on the struc-

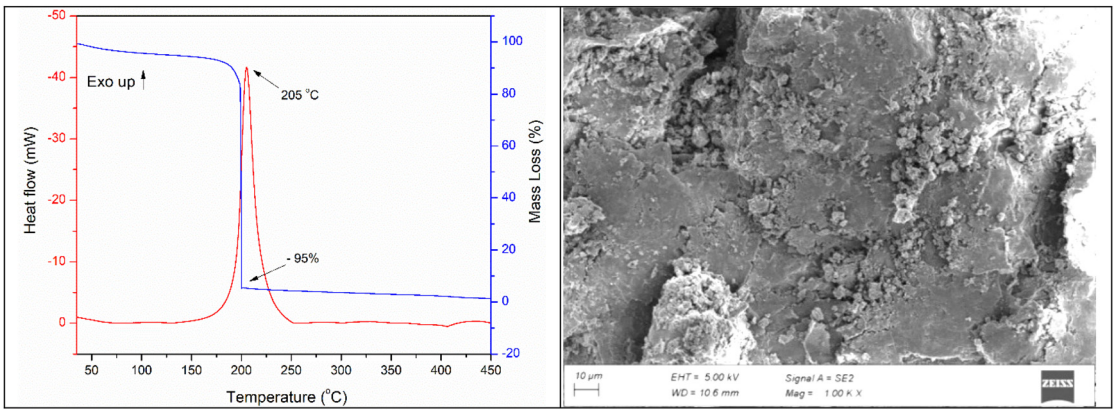

Fig. 14 (Left): DSC and TGA thermograms of **F1** formulation; (right): SEM image of **F1** formulation.

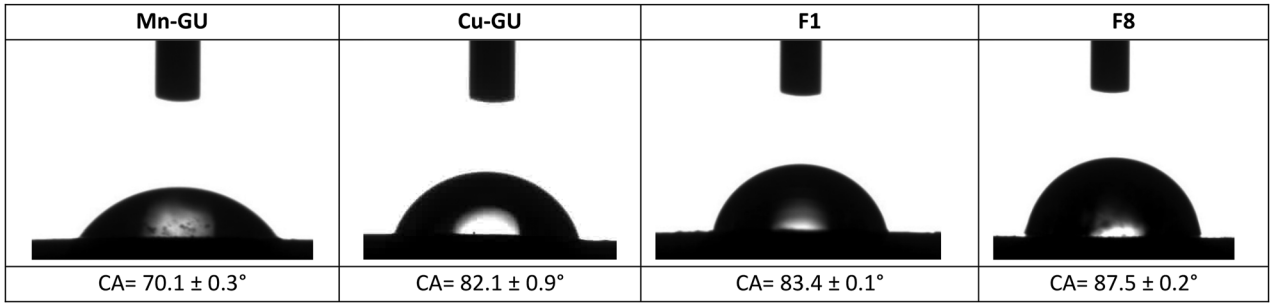

Fig. 15 Contact angles of **Mn–GU** and **Cu–GU** complexes and **F1** and **F8** formulations, all measured with deionized water.

ture and chemistry of this fuel surface, and how fast the liquid oxidizer can interact with the surface of the fuel. A fuel having hydrophilic surface can interact at a faster rate with highly polar oxidizers, such as H_2O_2, leading to rapid decomposition of H_2O_2 and thus to a shorter ID time.[54] The hydrophilicity or hydrophobicity (wettability) of a flat surface could be studied by contact-angle measurements, where a low contact angle (for example, with water) represents a more hydrophilic surface.[103] We studied the surface wettability of our complexes and formulations by the sessile-drop contact angle technique, where deionized water was used instead of H_2O_2 (Fig. 15). The water contact angles of **Mn–GU** and **Cu–GU** complexes were found to be 70.1°, and 82.1°, respectively. The lower contact angle of **Mn–GU** than that of **Cu–GU** could be attributed to the differences of their chemical structures and therefore to the differences of their surface structures. Due to the higher hydrophilicity of **Mn–GU**, its formulation **F1** also showed a relatively lower contact angle of 83.4° than that of the corresponding **Cu–GU** formulation **F8** (87.5°). The lower contact angle or better interaction of **F1** with H_2O_2 oxidizer was manifested in a shorter ID time than of **F8** formulation (Table 3). Moreover, the SEM images of **F1** and **F8** formulations showed that particles of both **Mn–GU** and **Cu–GU** complexes were evenly distributed over the surface of **NCH4**, making the surfaces of these formulations active for their hypergolic reactions with H_2O_2 (Fig. 14 and S20; ESI†).

Conclusions

We report a cost-effective methodology for the utilization of a biomass, available in huge quantities – coconut husk, and its conversion into inexpensive and sustainable rocket fuels (SRFs) – **NCH1–NCH4**. In addition to these SRFs, we also prepared **Mn–GU** or **Cu–GU** combustion catalysts, capable of promoting the hypergolic ignition of **NCH1–NCH4** fuels with an H_2O_2 (95%) oxidizer. **Mn–GU** or **Cu–GU** polymeric complexes were prepared in a single step from a guanine biomaterial and a simple salt of manganese or copper. The structures of **NCH1–NCH4** materials and **Mn–GU** and **Cu–GU** polymeric complexes were comprehensively characterized by FT-IR, UV-vis, XPS, and EPR spectroscopic analyses, elemental analysis, and SEM-EDS, DSC and TG analyses. Ignition studies of **F1–F11** formulations, containing **NCH1–NCH4** with **Mn–GU**, **Cu–GU**, or **JN15** complexes, with H_2O_2 (95%), showed impressive ID times down to 19 ms (for formulation **F10**), while EXPLO5 calculations of these formulations exhibited specific impulses up to 251 s and density specific impulses up to 354 s g cm^{-3}. High temperature stability studies of **F1** and **F8** formulations (without any added stabilizers) by isothermal TGA showed only 4.3% mass loss in both these formulations, which was 3.1 times lower than that of the military grade non-stabilized nitrocellulose. We believe that the presence of nitro-lignin and catalytic amounts of **Mn–GU** and **Cu–GU** polymeric complexes led to the improved thermostability of our formulations. Mechanistic studies showed that the degree of nitration of nitrocellulose in **NCH1–NCH4** SRFs, as well as MLC in **Mn–GU** and **Cu–GU** complexes played important roles in the hypergolic ignition processes of **F1–F8** formulations. Surface wettability (contact angle) studies of **Mn–GU** and **Cu–GU** complexes and **F1** and **F8** formulations showed that not only the chemical structures of the materials, but also their surface characteristics made contributions to the ignition properties of these materials, where the lower contact angle led to a shorter ID time. In conclusion, our valorization methodology of conversion of coconut husk into green hypergolic propellants, with an H_2O_2 oxidizer, is a conceptually new approach that can pave a way for the preparation of highly useful and economical sustainable rocket fuels (SRFs) from bio-waste and other bioresources.

Author contributions

Jagadish Das contributed to the supervision, analysis, resources, writing of the manuscript and funding acquisition. Ramlithin Mavila Chathoth synthesized and characterized the materials and wrote the manuscript. Charlie Oommen and Michael Gozin contributed to the resources and writing of the manuscript. Srinivas Dharavath, Manojkumar Jujam, and Deepan Chowdhury contributed to experimental characterization.

Data availability

The data supporting this article have been included as part of the ESI.†

Conflicts of interest

There are no conflicts to declare.

Acknowledgements

J. D. acknowledges financial support from the Department of Science and Technology, INSPIRE Division (Reference No. DST/INSPIRE/04/2022/000772), S. D. acknowledges SERB (ANRF) (No. CRG/2023/000007) and M. J. thanks PMRF for the fellowship. We acknowledge analytical support from I-STEM, CENSE IISc Bangalore, SATF IISc Bangalore, SSCU IISc Bangalore, SAIF IIT Madras, Department of Chemistry – IIT Patna, and SAIF IIT Patna. We also acknowledge Prof. Jagadeesh Gopalan for his help in carrying out the ignition tests.

References

1 O. Kodheli, N. Maturo, B. Shankar, J. C. M. Duncan, S. Chatzinotas, J. Querol and G. Goussetis, *IEEE Commun. Surv. Tutorials*, 2021, **23**(1), 70–109.
2 C. Schmierer, M. Kobald, K. Tomilin, U. Fischer and S. Schlechtriem, *Acta Astronaut.*, 2019, **159**, 578–583.
3 A. Acket-Goemaere, R. Brukardt, J. Klempner, A. Sierra and B. Stokes, In McKinsey & Company, 2024, **https://www.mckinsey.com/industries/aerospace-and-defense/our-insights/space-the-1-point-8-trillion-dollar-opportunity-for-global-economic-growth**.
4 M. Ross, D. Toohey, M. Peinemann and P. Ross, *Astropolitics*, 2009, **7**(1), 50–82.
5 A. Sarritzu and A. Pasini, *Acta Astronaut.*, 2024, **217**, 100–115.
6 R. G. Ryan, E. A. Marais, C. J. Balhatchet and S. D. Eastham, *Earth's Future*, 2022, **10**(6), e2021EF002612.
7 G. Silva and K. Iha, *J. Aerosp. Technol. Manage.*, 2012, **4**, 407.
8 I. I. Sam, S. Gayathri, G. Santhosh, J. Cyriac and S. Reshmi, *J. Mol. Liq.*, 2022, **350**, 118217.
9 S. M. Davis and N. Yilmaz, *Adv. Aerosp. Eng.*, 2014, 29313.
10 C. Hampton, K. Ramesh and J. Smith, *41st Aerospace Sci. Meeting and Exhibit*, 2003, 1359, DOI: **10.2514/6.2003-1359**.
11 S. A. Stern and J. T. Mullhaupt, *Chem. Rev.*, 1960, **60**(2), 185.
12 D. M. Mason, *J. Jet Propul.*, 1956, **26**(9), 741.
13 S. Li, H. Gau and J. M. Shreeve, *Angew. Chem.*, 2014, **126**, 3013.
14 H. M. Titi, J. M. Marrett, G. Dayaker, M. Arhangelskis, C. Mottillo, A. J. Morris, G. P. Rachiero, T. Friščić and R. D. Rogers, *Sci. Adv.*, 2019, **5**, 9044.
15 Q. Wang, J. Wang, S. Wang, Z. Wang, M. Cao, C. He, J. Yang, S. Zang and T. C. W. Mak, *J. Am. Chem. Soc.*, 2020, **142**, 12010.
16 H. M. Titi, M. Arhangelskis, G. P. Rachiero, T. Friscic and R. D. Rogers, *Angew. Chem., Int. Ed.*, 2019, **58**, 18399.
17 O. Jobin, C. Mottillo, H. M. Titi, J. M. Marrett, M. Arhangelskis, R. D. Rogers, B. Elzein, T. Friščić and E. Robert, *Chem. Sci.*, 2022, **13**, 3424.
18 S. Huang, W. Zhang, T. Liu, K. Wang, X. Qi, J. Zhang and Q. Zhang, *Chem. – Asian J.*, 2016, **11**, 3528–3533.
19 Q. Lai, Y. Long, P. Yin, J. M. Shreeve and S. Pang, *Acc. Chem. Res.*, 2024, 14031–14035.
20 T. L. Pu, X. Y. Wang, Z. B. Sun, X. Y. Dong, Q. Y. Wang and S. Q. Zang, *Angew. Chem., Int. Ed.*, 2024, **63**, e202402.
21 C. Wang, C. Li, Z. Duan, Z. F. Wang, Q. Y. Wang and S. Q. Zang, *Small*, 2024, **20**, 231097.
22 D. Trache, T. M. Klapötke, L. Maiz, M. A. Elghany and L. T. DeLuca, *Green Chem.*, 2017, **19**, 4711.
23 D. Freudenmann and H. K. Ciezki, *Propellants, Explos., Pyrotech.*, 2019, **44**, 1084–1089.
24 A. A. Esparza, R. E. Ferguson, A. Choudhuri, N. D. Love and E. Shafirovich, *Combust. Flame*, 2018, **193**, 417–423.
25 R. Amrousse, T. Katsumi, N. Itouyama, N. Azuma, H. Kagawa, K. Hatai, H. Ikeda and K. Hori, *Combust. Flame*, 2015, **162**(6), 2686–2692.
26 A. J. Bennett, L. M. Foroughi and A. J. Matzger, *J. Am. Chem. Soc.*, 2024, **146**, 1771–1775.
27 D. M. Le, A. Renault, A. Delage, P. Ducos, C. M. Sabate, N. Pelletier, E. Lacôte and G. Jacob, *Chem. – Eur. J.*, 2024, **30**, e202303965.
28 W. Florczuk and G. Rarata, *53rd AIAA/SAE/ASEE Joint Propul. Conf. AIAA*, 2017, 2017–4849.
29 D. A. Castaneda and B. Natan, *Acta Astronaut.*, 2019, **158**, 286–295.
30 V. K. Bhosale, J. Jeong and S. Kwon, *Fuel*, 2019, **255**, 115729.
31 M. A. Pfeil, A. S. Kulkarni, P. V. Ramachandran, S. F. Son and S. D. Heister, *J. Propul. Power*, 2016, **32**, 23–31.
32 M. A. Pfeil, J. D. Dennis, S. F. Son, S. D. Heister, T. L. Pourpoint and P. V. Ramachandran, *J. Propul. Power*, 2015, **31**, 365–372.
33 J. John, P. Nandagopalan, S. W. Baek and S. J. Cho, *Combust. Flame*, 2020, **212**, 205–215.
34 V. K. Bhosale, K. Lee, H. Yoon and S. Kwon, *Fuel*, 2024, **376**, 132688.
35 Y. J. Wang, X. Y. Wang, H. Xu, W. W. Ren, R. Pang, L. Yang, W. C. Tong, Q. Y. Wang and S. Q. Zang, *Chem. Eng. J.*, 2023, **455**, 140587.
36 J. H. Huang, A. Q. Ji, Z. Y. Wang, Q. Y. Wang and S. Q. Zang, *Adv. Sci.*, 2024, **11**, 2401861.
37 F. A. S. Mota, G. S. Dias, D. A. Machado, J. C. Andrade, F. S. Costa, L. Fei and C. Tang, *Combust. Flame*, 2024, **267**, 113567.
38 G. S. Dias, F. A. S. Mota, L. Fei, M. Liu, C. Tang and F. S. Costa, *Proc. Combust. Inst.*, 2024, **40**(1–4), 105269.
39 S. Nath, L. Mallick and J. K. Lefkowitz, *Combust. Flame*, 2023, **258**(2), 113061.

40 A. V. Shaferov, S. T. Arakelov, F. E. Teslenko, A. N. Pivkina, N. V. Muravyev and L. L. Fershtat, *Chem. – Eur. J.*, 2023, **29**, e202300948.
41 D. Zhang, D. Yu, Y. Yuan, P. Zhang and X. Fan, *Fuel*, 2023, **342**, 127788.
42 F. A. S. Mota, L. Fei, C. Tang, Z. Huang and F. S. Costa, *Fuel*, 2023, **336**, 127086.
43 S. C. Ricker, D. Brüggemann, D. Freudenmann, R. Ricker and S. Schlechtriem, *Fuel*, 2022, **328**, 125290.
44 K. Wang, Z. Wang, X. Zhao, X. Qi, S. Song, Y. Jin and Q. Zhang, *Combust. Flame*, 2022, **244**, 112235.
45 D. A. Castaneda and B. Natan, *Fuel*, 2022, **316**, 123432.
46 X. Zhao, Z. Wang, X. Qi, S. Song, S. Huang, K. Wang and Q. Zhang, *Inorg. Chem.*, 2021, **60**(22), 17033–17039.
47 F. Lauck, J. Balkenhohl, M. Negri, D. Freudenmann and S. Schlechtriem, *Combust. Flame*, 2021, **226**, 87–97.
48 M. B. Padwal, D. A. Castaneda and B. Natan, *Proc. Combust. Inst.*, 2021, **38**(4), 6703–6711.
49 K. Wang, T. Liu, Y. Jin, S. Huang, N. Petrutik, D. Shem-Tov, Q. Yan, M. Gozin and Q. Zhang, *J. Mater. Chem. A*, 2020, **8**, 14661–14670.
50 K. Wang, A. K. Chinnam, N. Petrutik, E. P. Komarala, Q. Zhang, Q. Yan, R. Dobrovetsky and M. Gozin, *J. Mater. Chem. A*, 2018, **6**, 22819–22829.
51 A. K. Chinnam, N. Petrutik, K. Wang, A. Shlomovich, O. Shamis, D. Shem-Tov, M. Suceska, Q. Yan, R. Dobrovetsky and M. Gozin, *J. Mater. Chem. A*, 2018, **6**, 19989–19997.
52 J. H. Corpening, R. K. Palmer, S. D. Heister and J. J. Rusek, *Int. J. Altern. Propul.*, 2007, **1**, 154–173.
53 A. A. Chandler, B. J. Cantwell, G. S. Hubbard and A. Karabeyoglu, *Acta Astronaut.*, 2011, **69**, 1066–1072.
54 N. Petrutik, I. Kaminker, E. Flaxer, D. Shem-Tov, T. Giladi, Y. Bar-Bechor, J. Das and M. Gozin, *Chem. Eng. J.*, 2023, **454**(2), 140170.
55 J. Das, D. Shem-Tov, S. Wang, L. Zhang, E. Flaxer, S. Zhang, J. Stierstorfer, K. Wang, Q. L. Yan, R. Dobrovetsky and M. Gozin, *Chem. Eng. J.*, 2021, **426**, 131806.
56 **https://www.iea.org/energy-system/renewables/bioenergy**.
57 M. G. Contreras, H. H. Escoto and E. A. Garnica, *Bioresour. Technol.*, 2023, **385**, 129470.
58 F. Cheng and C. E. Brewer, *Renewable Sustainable Energy Rev.*, 2017, **72**, 673–722.
59 N. Gaurav, S. Sivasankari, G. S. Kiran, A. Ninawe and J. Selvin, *Renewable Sustainable Energy Rev.*, 2017, **73**, 205–214.
60 M. A. A. El-Khair, S. A. Hanafi, M. G. A. El-Moghny, M. El-Saied, M. S. Elmelawy and M. S. El-Deab, *Chem. Eng. J.*, 2024, **490**, 151716.
61 C. Liu, P. Luan, Q. Li, Z. Cheng, P. Xiang, D. Liu, Y. Hou, Y. Yang and H. Zhu, *Adv. Mater.*, 2021, **33**, 2001654.
62 A. J. Ragauskas, G. T. Beckham, M. J. Biddy, R. Chandra, F. Chen, M. F. Davis, B. H. Davison, R. A. Dixon, P. Gilna, M. Keller, P. Langan, A. K. Naskar, J. N. Saddler, T. J. Tschaplinski, G. A. Tuskan and C. E. Wyman, *Science*, 2014, **344**, 1246843.
63 G. De Bhowmick, A. K. Sarmah and R. Sen, *Bioresour. Technol.*, 2018, **247**, 1144–1154.
64 D. Lee, H. Nam, M. W. Seo, S. H. Lee, D. Tokmurzin, S. Wang and Y. K. Park, *Chem. Eng. J.*, 2022, **447**, 137501.
65 C. Sawatdeenarunat, K. C. Surendra, D. Takara, H. Oechsner and S. K. Khanal, *Bioresour. Technol.*, 2015, **178**, 178–186.
66 A. R. Mankar, A. Pandey, A. Modak and K. K. Pant, *Bioresour. Technol.*, 2021, **334**, 125235.
67 N. Chalmpes, M. Baikousi, T. Giousis, P. Rudolf, C. E. Salmas, D. Moschovas, A. Avgeropoulos, A. B. Bourlinos, I. Tantis, A. Bakandritsos, D. Gournis and M. A. Karakassides, *Micro*, 2022, **2**, 137–153.
68 **https://www.fao.org/faostat/en/#data/QCL**.
69 S. O. Anuchi, K. L. S. Campbell and J. P. Hallett, *Sci. Rep.*, 2022, **12**, 6108.
70 E. Colacio, O. Crespo, R. Cuesta, R. Kivek and A. Lagun, *J. Inorg. Biochem.*, 2004, **98**, 595–600.
71 C. M. Mikulski, L. Mattucci, Y. Smith, T. B. Tran and N. M. Karyannis, *Inorg. Chim. Acta*, 1982, **66**, L71–L73.
72 T. F. Mastropietro, D. Armentano, E. Grisolia, C. Zanchini, F. Lloret, M. Julve and G. De Munno, *Dalton Trans.*, 2008, **4**, 514–520.
73 A. P. Novikov, M. A. Volkov, A. V. Safonov, M. S. Grigoriev and E. V. Abkhalimov, *Crystals*, 2021, **11**, 1417.
74 M. Rohner, A. Medina-Molner and B. Spingler, *Inorg. Chem.*, 2016, **55**, 6130–6140.
75 M. Orts-Arroyo, N. Moliner, F. Lloret and J. Martínez-Lillo, *Magnetochemistry*, 2022, **8**, 93.
76 W. Z. Wang, C. K. Xu, G. H. Wang, Y. K. Liu and C. L. Zheng, *Adv. Mater.*, 2002, **14**(11), 837–840.
77 M. P. R. Guambo, L. Spencer, N. S. Vispo, K. Vizuete, A. Debut, D. C. Whitehead, R. Santos-Oliveira and F. Alexis, *Polymers*, 2020, **12**, 3042.
78 M. Ichim, L. Stelea, I. Filip, G. Lisa and E. Ioan Muresan, *Crystals*, 2022, **12**, 1249.
79 B. R. Freitas, J. O. Braga, M. P. Orlandi, B. P. da Silva, I. V. Aoki, V. F. C. Lins and F. Cotting, *J. Mater. Res. Technol.*, 2022, **19**, 1332–1342.
80 V. I. Kovalenko, R. M. Mukhamadeeva, L. N. Maklakova and N. G. Gustova, *J. Struct. Chem.*, 1994, **34**, 540–547.
81 H. Váquez-Torres, G. Canché-Escamilla and C. A. Cruz-Ramos, *J. Appl. Polym. Sci.*, 1992, **45**, 633–644.
82 C. M. Mikulski, L. Mattucci, L. Weiss and N. M. Karayannis, *Inorg. Chim. Acta*, 1985, **107**(1), 81–85.
83 J. Ruwoldt, M. Tanase-Opedal and K. Syverud, *ACS Omega*, 2022, **7**(50), 46371–46383.
84 Y. G. Khabarov, N. Y. Kuzyakov, V. A. Veshnyakov, G. V. Komarova and A. Y. Garkotin, *Russ. Chem. Bull.*, 2016, **65**, 2925–2931.
85 P. Makuła, M. Pacia and W. Macyk, *J. Phys. Chem. Lett.*, 2018, **9**(23), 6814–6817.

86 T. Li, J. Xu, J. Han and Y. He, *Micromachines*, 2021, **12**, 1378.
87 D. M. Gagnon, R. C. Hadley, A. Ozarowski, E. M. Nolan and R. D. Britt, *J. Phys. Chem. B*, 2019, **123**(23), 4929–4934.
88 M. S. Reddya, B. Prathimaa, M. Saraswathib, S. Babuc, Y. Saralad and A. V. Reddy, *J. Appl. Pharm. Sci.*, 2016, **6**(05), 090–096.
89 Ş. Ç. Özkan, A. Yilmaz, E. Arslan, L. Açık, Ü. Sayın and E. G. Mutlu, *Supramol. Chem.*, 2014, **27**(4), 255–267.
90 M. Li, W. Lei, Y. Yu, W. Yang, J. Li, D. Chen, S. Xu, M. Fenga and H. Li, *Nanoscale*, 2018, **10**, 15926–15931.
91 A. Ghods, C. Zhou and I. T. Ferguson, *J. Vac. Sci. Technol., A*, 2020, **38**, 042408.
92 S. Ptasińska, A. Stypczyńska, T. Nixon, N. J. Mason, D. V. Klyachko and L. Sanche, *J. Chem. Phys.*, 2008, **129**, 065102.
93 H. Zhou, H. Xu and Y. Liu, *Appl. Catal., B*, 2019, **244**, 965–973.
94 Z. Yang, J. Gong, C. Tang, W. Zhu, Z. Cheng, J. Jiang, A. Ma and Q. Ding, *J. Mater. Sci.: Mater. Electron.*, 2017, **28**, 17533–11754.
95 M. Ganiga and J. Cyriac, *ChemPhysChem*, 2016, **17**, 2315–2321.
96 M. Fujiwara, T. Matsushita and S. Ikeda, *Anal. Sci.*, 1993, **9**, 289–291.
97 R. Mrozek, Z. Rzączyńska and M. Sikorska-Iwan, *J. Therm. Anal. Calorim.*, 2001, **63**, 839–846.
98 D. Frem, *J. Aerosp. Technol. Manage.*, 2018, **10**, e3318.
99 S. N. A. Rusly, S. H. Jamal, A. Samsuri, S. A. M. Noor and K. S. A. Rahim, *Energ. Mater. Front.*, 2024, **5**(1), 52–69.
100 M. F. Cherif, D. Trache, F. Benaliouche, A. F. Tarchoun, S. Chelouche and A. Mezroua, *Int. J. Biol. Macromol.*, 2020, **164**, 794–807.
101 M. F. Rosa, E. S. Medeiros, J. A. Malmonge, K. S. Gregorski, D. F. Wood, L. H. C. Mattoso, G. Glenn, W. J. Orts and S. H. Imam, *Carbohydr. Polym.*, 2010, **81**(1), 83–92.
102 R. Serra-Maia, M. Bellier, S. Chastka, K. Tranhuu, A. Subowo, J. D. Rimstidt, P. M. Usov, A. J. Morris and F. M. Michel, *ACS Appl. Mater. Interfaces*, 2018, **10**, 21224–21234.
103 T. Huhtamäki, X. Tian, J. T. Korhonen and R. H. A. Ras, *Nat. Protoc.*, 2018, **13**(7), 1521–1538.